Faraday Discussions

Accepted Manuscript

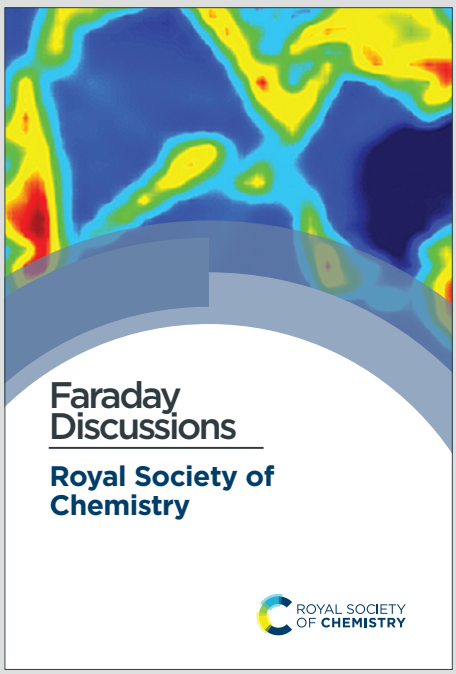

This article can be cited before page numbers have been issued, to do this please use: D. J. Romano, B. H. Savitzky, A. M. Carrascosa, A. Narkiewicz-Jodko, J. D. Geiser, P. Y. Wang, L. Huang, S. W. Crane, X. Cheng, M. Liang, S. Mous, M. P. Minitti, M. Simmermacher, A. Kirrander and P. M. Weber, *Faraday Discuss.*, 2026, DOI: 10.1039/D6FD00068A.

ROYAL SOCIETY OF CHEMISTRY

www.rsc.org/faraday_d

View Article Online
DOI: 10.1039/D6FD00068A

Journal Name

ARTICLE TYPE

Cite this: DOI: 00.0000/xxxxxxxxxx

Spectrally Resolved X-Ray Scattering

David J. Romano[a], Benjamin H. Savitzky[a], Andrés Moreno Carrascosa[b], Alexander Narkiewicz-Jodko[a], Joseph D. Geiser[a], Patrick Yuheng Wang[b], Lisa Huang[a], Stuart W. Crane[a], Xinxin Cheng[c], Mengning Liang[c], Sandra Mous[c], Michael P. Minitti[c], Mats Simmermacher[b], Adam Kirrander[a,b*], and Peter M. Weber[a*]

Received Date
Accepted Date

DOI: 00.0000/xxxxxxxxxx

The Bethe surface represents the X-ray scattering cross section as a function of momentum transfer and energy loss, mapping the electronic spectrum of the target via the inelastic transition matrix elements. By effectively merging spectroscopy and scattering, a time-resolved measurement of the molecular Bethe surface during a chemical reaction could reveal details of the reaction path through the manifolds of electronic states and conical intersections. However, conventional imaging detectors used for X-ray scattering lack energy resolution. We demonstrate here how the Bethe surface can be measured with the help of a spectral filter in the form of a thin zinc metal foil inserted between the target and the detector. Harnessing the inherent stochasticity of X-ray pulses generated by self-amplified spontaneous emission at X-ray free electron lasers (XFELs), we demonstrate how the double differential X-ray scattering cross section can be reconstructed using a novel ghost imaging algorithm. Corrections for fluorescence from the metal filter need to be applied. The method requires excellent signal levels that can be obtained for molecules with large scattering cross sections, but advances in XFEL technology promise opportunities for a wide range of applications.

1 Introduction

The study of gas-phase molecular structure and dynamics has been profoundly advanced by the emergence of X-ray free-electron lasers (XFELs).[1–3] These novel instruments now enable time-resolved gas-phase experiments, achieving excellent spatial and temporal resolution with high signal-to-noise ratios. X-ray scattering experiments have observed molecular evolution on ultrashort time scales upon optical excitation, revealing subtle electronic and nuclear effects.[4–6] Recent developments also include the measurement of intramolecular charge transfer, the observation of nuclear dynamics, and determination of the orientation of transition dipole moment.[7–13]

Conventional imaging detectors lack energy resolution and conflate elastic and inelastic scattering. This detector-level energy integration obscures subtle effects of electronic structure on the scattering signal, effectively hiding energy-resolved observables. We will present in this paper an approach for retrieving such information using existing energy-integrating detectors. Non-resonant X-ray scattering can be expressed in terms of a double-differential X-ray scattering cross section (DDSCS). The DDSCS depends on the solid angle Ω and the energy loss $\Delta E = E_\mathrm{i} - E_\mathrm{s}$, obtained as the energy difference between the initial and the scattered photon. Within the Waller-Hartree approximation, the DDSCS is expressed as[14–16]

$$\frac{d^2\sigma}{d\Omega d\Delta E} = \left(\frac{d\sigma}{d\Omega}\right)_\mathrm{Th} \sum_\beta \left|\langle\Psi_\beta|\hat{L}|\Psi_\alpha\rangle\right|^2 \delta(E_\beta - E_\alpha - \Delta E), \quad (1)$$

with $(d\sigma/d\Omega)_\mathrm{Th}$ the Thomson scattering cross section of a free electron,

$$\left(\frac{d\sigma}{d\Omega}\right)_\mathrm{Th} = r_0^2 |\boldsymbol{\epsilon}_\mathrm{i} \cdot \boldsymbol{\epsilon}_\mathrm{s}^*|^2, \quad (2)$$

where r_0 is the classical electron radius and $|\boldsymbol{\epsilon}_\mathrm{i} \cdot \boldsymbol{\epsilon}_\mathrm{s}^*|^2$ is the polarization factor for the incident and scattered radiation. Returning to Eq. (1), Ψ_α and Ψ_β are the initial and final states with their respective energies E_α and E_β. The $\hat{L}$ is the scattering operator,

$$\hat{L} = \sum_{j=1}^{N_\mathrm{el}} e^{\imath \boldsymbol{q}\cdot\boldsymbol{r}_j}, \quad (3)$$

with the sum running over all N_el electrons j, and the momentum transfer vector $\boldsymbol{q} = \boldsymbol{k}_\mathrm{i} - \boldsymbol{k}_\mathrm{s}$ is the difference between the incident and scattered wave vectors.

Gas-phase X-ray scattering experiments at XFELs are performed using energy-integrating area detectors that record the total scattering $d\sigma/d\Omega$ only.[17] This total X-ray scattering involves a sum over *all* possible transitions between the initial and final elec-

[a] Department of Chemistry, Brown University, Providence, RI 02912, USA.
[b] Department of Chemistry, University of Oxford, Oxford, OX1 3QZ, UK.
[c] *Linac Coherent Light Source, SLAC National Accelerator Laboratory, Menlo Park, CA 94025, USA.*

View Article Online
DOI: 10.1039/D6FD00068A

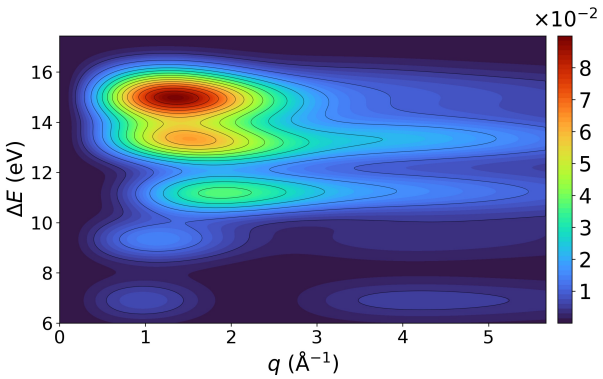

Fig. 1 Theoretical Bethe surface of the water molecule. Calculated Bethe surface for the water molecule H_2O depicting the first 20 inelastic scattering transitions calculated with ADC(2)/aug-cc-pVDZ+Rydberg.

tronic states. Based on the completeness of the sum over states, this then reduces to a measurement of the initial state only.[14] This is not necessarily bad, and as discussed above, a wide range of important and highly relevant information can be retrieved from such experiments.[18–20] At the same time, it is clear that highly valuable information about excited states is lost in the process.

This information would be available from spectrally resolved X-ray scattering measurements, where the individual inelastic components that contribute to the total X-ray scattering signal are isolated and characterized as a function of the momentum transfer q and the energy loss ΔE. This spectrally resolved scattering signal would provide deeper insight into the molecular electronic landscape and bridge the gap between scattering and spectroscopy. Experimental implementations that record X-ray scattering patterns with spectral resolution would therefore mark a major advance in scattering methodology.

Figure 1 illustrates this theoretically for the water molecule by graphing the scattering signal as a function of energy loss and the absolute value of the momentum transfer vector in what is called a *Bethe surface*.[21] With an assumed energy resolution of 0.56 eV, it includes the inelastic X-ray scattering signals of the first 20 singlet excited states of H_2O, calculated at the second-order algebraic diagrammatic construction level of theory[22] with the augmented correlation-consistent polarized valence double-zeta basis set[23,24] supplemented with Rydberg functions from Kaufmann *et al.*[25], hereafter denoted ADC(2)/aug-cc-pVDZ+Rydberg. The distinct features of each transition are immediately apparent. The magnitude of these inelastic X-ray signals is proportional to the generalized oscillator strength of the excitation[26], while the positions of the maxima are closely related to the orbital overlap dominating the transition.

Full characterization of the Bethe surface requires spectrally separating these components and has been historically achieved with energy-resolving detectors with limited solid-angle coverage[27] or indirect estimation using independent-atom model (IAM) calculations to approximate and subtract the inelastic background.[28] Neither approach is fully satisfactory: the former sacrifices counting statistics and abandons q resolution, while the latter presupposes the very electronic structure one wishes to measure. Most early investigations of the Bethe surface have therefore employed electron scattering,[29] even though it remains difficult to spectrally analyze the electron energy spectrum with modern imaging detectors.

In this work, we present a new method for the direct, model-independent, experimental spectral separation of total X-ray scattering signals, which we implemented at the Linac Coherent Light Source (LCLS). By developing a spectral ghost-imaging technique, we exploit the intrinsic shot-to-shot spectral stochasticity of self-amplified spontaneous emission (SASE) pulses in conjunction with a thin zinc foil acting as a spectral filter. Correlation of the measured scattering intensities with independently recorded pulse spectra allows reconstruction of the energy-resolved scattering profile from measurements made with a conventional energy-integrating detector. Here we describe the experimental and analytical methodology, including preprocessing, correction for fluorescence from the zinc foil, and the ghost-imaging spectral signal inversion, and demonstrate successful application of the technique on gas-phase SF_6.

2 Methods

2.1 Experimental Details

The linearly polarized 120 Hz, ~ 25 fs (FWHM), ~ 1.5 mJ primary beam of the LCLS with a nominal photon energy of 9.66 keV was focused using Kirkpatrick-Baez mirrors into a windowless gas flow cell with a beryllium out-coupling window that minimized absorption and re-scattering. The gas-phase sample of sulfur hexafluoride was held at ~ 20 Torr. A 15 μm thick sheet of zinc foil was placed ~ 3.8 mm after the beryllium window normal to the primary beam, occluding about half of the detector. The scattered X-rays were detected with a Jungfrau-4M hard X-ray detector with a pixel size of 75 μm × 75 μm situated ~ 9.5 cm behind the scattering cell. In addition, before entering the scattering cell, a small fraction of the primary beam was directed to a bent-crystal hard X-ray single-shot spectrometer (HXSSS) using the Si(110) crystal for a (440) reflection.[30,31] Shortly upstream of the scattering cell, the primary beam was directed through a thin SiN crystal. The intensity of the Compton back-scattering from this crystal was measured via 8 diodes. This setup, known as the intensity position monitor (IPM), was used as an in-line nondestructive measurement of the number of photons in each pulse.[32] The experimental setup is depicted in Fig. 2.

2.2 Preprocessing

Two-dimensional scattering patterns from the Jungfrau-4M detector were recorded on a shot-by-shot basis. Each image was gain-corrected to a readout in analog-to-digital units (ADU), closely related to the X-ray photon energy. For each image, the ADU readings were thresholded to remove dark counts, sample fluorescence, and other spurious signals while preserving the integrity of the scattering data. A mask was applied to each image to remove overactive or bad pixels from the analysis. For this experiment, the mask removed ~6% of all pixels.

The high-intensity X-ray pulses were excluded from the cali-

View Article Online
DOI: 10.1039/D5FD00068A

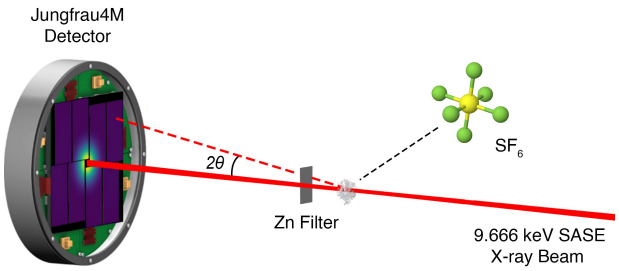

Fig. 2 Experimental Setup. SASE X-ray pulses from the LCLS are focused onto a gas-phase sample of sulfur hexafluoride, SF_6. A zinc foil is placed in front of one side of the scattering cell, filtering half of the post-specimen scattered photons before they hit the detector. The signal on both the filtered and unfiltered sides are recorded with a Jungfrau-4M Detector.

bration steps to remove absorption-scattering events by setting the threshold based on deviation from kinematical theory. The unfiltered portion of the two-dimensional scattering pattern was used to determine the detector position by fitting a theoretical total scattering pattern of SF_6, calculated with in-house scattering code[18,19,33] at the coupled-cluster singles and doubles level of theory[34] with the augmented correlation-consistent polarized valence double-zeta basis set, CCSD/aug-cc-pVDZ. The fitting process iteratively accounts for the correction factors addressed in reference[17], the variation of the Thomson scattering cross section with respect to the X-ray polarization, and physical geometry of the Jungfrau-4M detector. Once the optimal detector center and distance were found, each image was divided into the unfiltered and filtered portions, azimuthally averaged, and transformed into momentum space to produce two one-dimensional scattering profiles for each shot.

Using the data from the IPM, HXSSS, and the filtered and unfiltered azimuthally averaged scattering signals, specific shots were removed to eliminate incomplete or damaged data.

2.3 Accounting for zinc fluorescence and shot-by-shot variations

The experimental setup for spectral ghost imaging requires that a metal foil be placed in front of the main scattering cell with the specific purpose of blocking a fraction of the scattering as a function of photon energy. However, some of the absorbed photons may be re-emitted as fluorescence, which may impinge on the detector. In our case, the zinc K_α and K_β fluorescence emission lines are not removed by the ADU threshold and add spurious signal. Therefore, it is necessary to determine and correct for the impact of the fluorescence signal on the final result. To do so, we first calculate the intensity of the scattered radiation on the zinc foil and then evaluate the amount of fluorescence from each pixel element of the foil. The fluorescence intensity measured by the detector is then obtained by summing the emission contributions from all pixel elements of the metal foil.

We start with an *ab initio* scattering pattern calculated via our in-house code.[18] This software produces a one-dimensional differential scattering pattern $d\sigma/d\Omega$. In this form, the total differential X-ray scattering cross section has been normalized by the Thomson scattering cross section for an electron σ_{Th}. Therefore, the units of $d\sigma/d\Omega$ are inverse steradians, sr^{-1}.

To determine the scattering occurring in a given pixel element on a surface normal to the optical axis, the *ab initio* differential cross section must be multiplied by a prefactor $d\Omega$ that converts to units of area while accounting for off-axis pixels' reduced effective cross sections and for the inverse-square law intensity dependence. This prefactor is given by

$$d\Omega(2\theta) = \frac{dxdy}{z^2}\cos^3(2\theta), \tag{4}$$

where dx and dy are the pixel's x and y extents, z is the normal distance from the source to the surface, and 2θ is the polar angle of scattering relative to the incident beam.

Further, the incident beam is linearly polarized, requiring an additional, ϕ-dependent polarization factor,

$$C_{\mathrm{Th}}(2\theta,\phi) = \sin^2(\phi) + \cos^2(2\theta)\cos^2(\phi), \tag{5}$$

where ϕ is the azimuthal angle relative to the photon polarization. Combining these together, the exposure of a zinc pixel with coordinate $(2\theta,\phi)$, area $dxdy$, normal distance z, and incident photon energy E_{i} is given by the effective cross section

$$d\sigma_{\mathrm{eff}}(E_{\mathrm{i}},2\theta,\phi) = d\Omega(2\theta)C_{\mathrm{Th}}(2\theta,\phi)\frac{d\sigma(E_{\mathrm{i}},2\theta)}{d\Omega}. \tag{6}$$

Fluorescence by itself is a completely isotropic emission process. However, one can imagine a situation where the absorption and fluorescence happen at the very beginning of the zinc foil; then, the fluoresced light must travel through the rest of the foil to reach the detector. As the path length through the foil is different for every fluorescence polar angle θ', differing fractions of fluoresced light will be reabsorbed as a function of that angle, therefore the resultant "fluorescence pattern" becomes anisotropic in θ'. To determine the fluorescence pattern emitted by each normal pixel element on the zinc foil, we start by calculating the amount of light incident on a length element dL at depth L through the zinc, where both dL and L are normal to the surface of the zinc foil. This process follows the Lambert-Beer law:

$$d\sigma_L(E_{\mathrm{i}},2\theta,\phi,L) = d\sigma_{\mathrm{eff}}(E_{\mathrm{i}},2\theta,\phi)\exp\left(\frac{-L}{\lambda(E_{\mathrm{i}})\cos(2\theta)}\right), \tag{7}$$

where $\lambda(E)$ is the attenuation length of the zinc at energy E. The amount of light absorbed through the length element dL is the negative rate of change of $d\sigma_L(E_{\mathrm{i}},2\theta,\phi,L)$ with respect to L. A fraction of this absorbed light, η, will be fluoresced. This fraction is found by using the following formula,

$$\eta = \omega_{\mathrm{K}} J_{\mathrm{K}} \approx 0.422, \tag{8}$$

where ω_{K} is the K-shell fluorescence yield and J_{K} is the K-shell jump factor for zinc. Only the K-shell is considered here as less energetic fluorescence emissions are filtered by the ADU threshold of the Jungfrau-4M detector. The fluoresced light is spread over 4π steradians, and attenuated by the length of zinc it passes

View Article Online
DOI: 10.1039/D6FD00068A

before traveling to the detector. This remaining distance depends on the fluorescence polar angle θ', but is isotropic in the fluorescence azimuthal angle ϕ'. Therefore, the differential fluorescence pattern for a given length element dL inside a pixel $(2\theta, \phi)$ is

$$\frac{\partial\sigma_{\text{fl}}(E_{\text{i}}, 2\theta, \phi, \theta', \phi', L)}{\partial\Omega'} dL = \frac{\eta e^{\frac{-(L_z - L)}{\lambda(E_{\text{fl}})\cos(\theta')}}}{4\pi} \times \frac{-d\sigma_L(E_{\text{i}}, 2\theta, \phi, L)}{dL} dL, \tag{9}$$

where L_z is the thickness of the zinc foil, and E_{fl} is the fluorescence photon energy. Finally this term is then integrated over all possible fluorescence depths within the zinc foil to give an expression for the total differential fluorescence pattern emanating from a given (x,y) position on the zinc foil,

$$\frac{\partial\sigma_{\text{fl}}(E_{\text{i}}, 2\theta, \phi, \theta', \phi')}{\partial\Omega'} = \int_0^{L_z} \frac{\eta e^{\frac{-(L_z - L)}{\lambda(E_{\text{fl}})\cos(\theta')}}}{4\pi} \times \frac{-d\sigma_L(E_{\text{i}}, 2\theta, \phi, L)}{dL} dL. \tag{10}$$

This integral can be solved analytically, giving the final expression,

$$\frac{\partial\sigma_{\text{fl}}(E_{\text{i}}, 2\theta, \phi, \theta', \phi')}{\partial\Omega'} = \frac{d\sigma_{\text{eff}}(E_{\text{i}}, 2\theta, \phi)\eta\lambda(E_{\text{fl}})\cos(\theta')}{4\pi[\lambda(E_{\text{i}})\cos(2\theta) - \lambda(E_{\text{fl}})\cos(\theta')]} \times \left(e^{-L_z/[\lambda(E_{\text{i}})\cos(2\theta)]} - e^{-L_z/[\lambda(E_{\text{fl}})\cos(\theta')]}\right). \tag{11}$$

To find the total accumulation of fluorescence on the detector the zinc foil is discretized into pixels in the normal direction, Eq. (11) is calculated for each of these zinc pixels, and the output fluorescence is propagated from each zinc pixel to the detector. There is no polarization factor in this case as the fluoresced light is unpolarized. The total fluorescence on a given detector pixel is then

$$d\sigma_{\text{fl}}(E_{\text{i}}, \theta', \phi') = \sum_{(x,y)\in\text{Zn}} d\Omega'(\theta') \times \frac{d\sigma_{\text{fl}}(E_{\text{i}}, 2\theta, \phi, \theta', \phi')}{d\Omega'} \tag{12}$$

Note that here, the prefactor $d\Omega'$ is different than in Eq. (6). In Eq. (6), $dxdy$ refers to the pixel size chosen to discretize the zinc foil for the calculation, and z refers to the normal distance from the scattering cell to the zinc foil. Here, when Eq. (4) is used to determine $d\Omega'$, $dxdy$ is the pixel size on the detector, and z is the normal distance from the zinc to the detector.

This entire process thus far assumes that the scattering signal originates from a single point. However, there is a roughly 2 mm long scattering volume, and many of the geometric parameters change when the scattering source location is changed. Therefore, the signal must be integrated across the entire scattering length. The final amount of incident fluorescence intensity with respect to the simulated scattering intensities is shown in Fig. 3.

To determine the effect of this fluorescence for the unfiltered and filtered azimuthal averages on any given shot with spectrum $m(E_{\text{i}})$, ratios were taken from these simulation results of the azimuthal averaged of the filtered scattering signal to the azimuthal average of the filtered scattering with fluorescence, and likewise for the unfiltered signal. These two curves are shown in Fig. 4. Fluorescence from the K-shell can occur only if the incident photon energy is above the zinc K-edge. The parts of the SASE pulse with energies below the K-edge will not produce fluorescence. Therefore, correction matrices were created containing the fluorescence ratio curves above the K-edge, and unity everywhere else. Dot products of the correction matrices were taken with the incident spectra to determine a shot-to-shot correction factor for the filtered and unfiltered azimuthally averaged signals. These correction factors were then multiplied element-wise to the shot-to-shot azimuthally average signals before proceeding with the ghost-imaging step of the analysis.

3 Results and Discussion

3.1 Spectral Ghost Imaging

Ghost imaging, which was originally developed for quantum systems in the spatial domain,[35–45] correlates a beam passing through an object of study and measured on a "bucket" (*i.e.* integrating) detector that has no spatial resolution with a reference beam that is measured with spatial resolution but never encounters the object. The general ghost imaging concept has been mapped onto other domains, for example the time domain to resolve ultrafast time-dependent processes.[46] Here, we adapt the scheme to the energy domain in order to spectrally resolve the total scattering signal by taking a pre-sample shot-by-shot measurement of the X-ray spectrum as a reference signal, while using each pixel of the imaging detector as a bucket detector with no resolution in energy.

The spectral decomposition of the scattering signal exploits stochastic fluctuations of the SASE pulses from the LCLS XFEL. On a shot-by-shot basis, the spectra of the X-ray pulses fluctuate over a ~ 25 eV (FWHM) range as illustrated in Fig. 5. For each shot j, the measured scattering intensity $d_j(q)$ is given by

$$d_j(q) = \int_0^\infty m_j(E_{\text{i}}) \int_{-\infty}^\infty \frac{d^2\sigma}{d\Omega d\Delta E}\, d\Delta E\, dE_{\text{i}}, \tag{13}$$

where $m_j(E_{\text{i}})$ is the energy spectrum of incident pulse j. The integral over ΔE reflects that the detector lacks energy resolution. Note that the DDSCS and ghost-imaging framework are formulated in terms of the momentum transfer q, as this dictates the intrinsic scattering physics of the sample and is the natural description in the molecular frame. However, the experimental data is measured in the laboratory frame at fixed polar, 2θ and azimuthal, ϕ, scattering angles. As discussed in Section 2.3, the spurious fluorescence signals are also highly dependent on the experimental geometry. Therefore, the fluorescence corrections and pre-processing are carried out in the laboratory frame. Once these artifacts are corrected, the signals are cast onto a common q-grid via the relation $q = 4\pi/\lambda \sin\theta$ before proceeding with the ghost-imaging analysis.

Importantly, the integral over ΔE in Eq. (13) destroys the energy-dependent information, such that spectral separation of the total scattering is no longer possible in a traditional diffraction experiment. To apply our ghost-imaging method for recovering this information, the zinc foil that covers approximately half of the scattering detector serves as a spectral filter. The center of the incident photon energy is tuned just above the Zn K-edge, such that the filter transmission $f(E_{\text{s}})$ is large for photons with

View Article Online
DOI: 10.1039/D6FD00068A

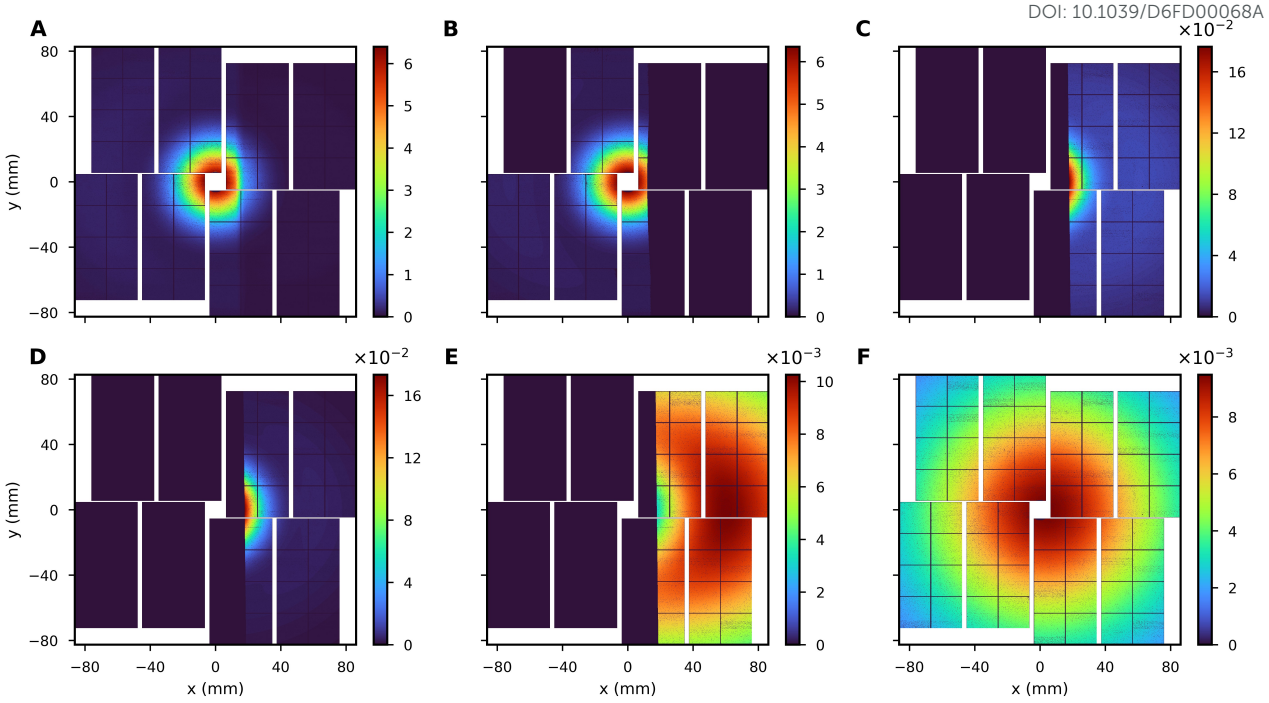

Fig. 3 Scattering of SF_6 and Zn fluorescence. (**A**) Experimental scattering. Filtered region of the detector is seen on the right hand side. (**B**) Simulated unfiltered total scattering. (**C**) Simulated filtered total scattering. (**D**) Simulated filtered elastic scattering. (**E**) Simulated filtered inelastic scattering. (**F**) Simulated zinc K-shell fluorescence. The color scale is in arbitrary intensity units and masked pixels are represented as 0.

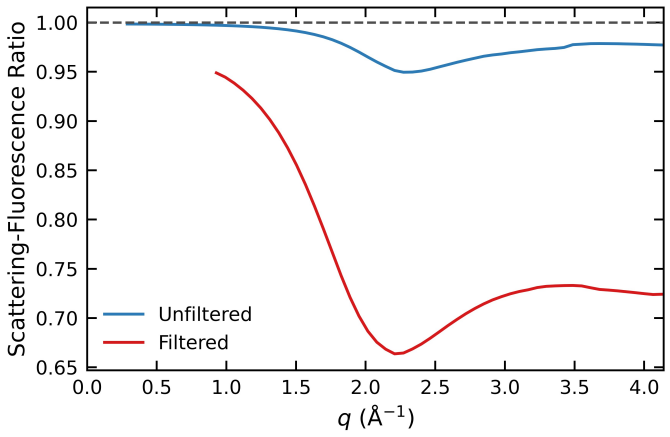

Fig. 4 Zinc fluorescence ratios. For the unfiltered and filtered sides of the detector, the scattered light is expressed as a fraction of the total signal (scattering and fluorescence from the zinc foil) incident on the detector. The filtered portion does not extend as low in q as the unfiltered curve due to the geometry of the Zn-filter.

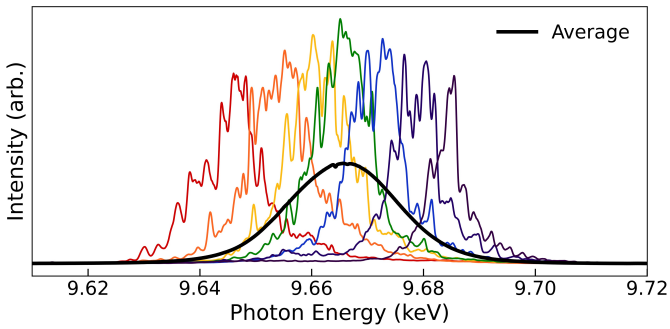

Fig. 5 LCLS X-ray Spectra. Seven representative spectra of individual SASE pulses. The average spectra of all pulses in the dataset is shown in black. The spectral incoherency and stochastic fluctuations enable the reconstruction of the inelastic and elastic X-ray scattering by ghost imaging.

$\Delta E > 0$ and small otherwise. Incident X-ray pulse spectra $m_j(E_\mathrm{i})$ are measured with the pre-scattering cell HXSSS alongside the scattering signal on the unfiltered and Zn-filtered halves of the detector, yielding a pulse energy spectrum and two complementary scattering (half) images for each shot.

In the presence of the Zn filter, the scattering intensity in Eq. (13) becomes

$$d'_j(q) = \int_0^\infty m_j(E_\mathrm{i}) \int_{-\infty}^\infty f(E_\mathrm{s}) \frac{d^2\sigma(q,\Delta E)}{d\Omega d\Delta E} d\Delta E \, dE_\mathrm{i}$$

$$= \int_0^\infty m_j(E_\mathrm{i}) a(q,E_\mathrm{i}) dE_\mathrm{i} \qquad (14)$$

where $d'_j(q)$ is the filtered scattering intensity and

View Article Online
DOI: 10.1039/D6FD00068A

$$a(q,E_\mathrm{i}) = \left(f(E_\mathrm{s}) * \frac{d^2\sigma(q,\Delta E)}{d\Omega d\Delta E} \right)(E_\mathrm{i}) \tag{15}$$

is the dynamic structure factor convolved in energy with the filter function. In the absence of a filter, the filter function reduces to $f(E_\mathrm{s}) = 1$ and we revert to Eq. (13).

The ghost-imaged object is the quantity $a(q,E_\mathrm{i})$. To recover $a(q,E_\mathrm{i})$, we divide the momentum-transfer range into small q-bins and treat each bin as a bucket, then extract $a(q_0,E_\mathrm{i})$ for every discrete value of q_0. With a large number of measurements N_j and with N_ϵ energy bins, we define $d'_j \rightarrow \boldsymbol{d'} \in \mathbb{R}^{N_j}$, $m_j(E_\mathrm{i}) \rightarrow \boldsymbol{M} \in \mathbb{R}^{N_j \times N_\epsilon}$, and $a(E_\mathrm{i}) \rightarrow \boldsymbol{a} \in \mathbb{R}^{N_\epsilon}$, and form the equation

$$\boldsymbol{d'} = \boldsymbol{M} \cdot \boldsymbol{a}, \tag{16}$$

which is the discretized form of Eq. (14) taken over all shots $j \in N_j$. Provided sufficient signal levels, Eq. (16) can be inverted to retrieve $\boldsymbol{a}$ over the energy range sampled by the stochastic SASE pulses.

In practice, shot-to-shot intensity variations as well as slower variations in the gas flow (and thus sample density) will impart artifacts in the spectral correlation when determining $\boldsymbol{a}$. These variations must therefore be removed before proceeding with the ghost-imaging analysis. To do so, the ratio of the filtered to unfiltered azimuthally averaged scattering was used in place of $\boldsymbol{d'}$ in the ghost-imaging analysis. Simply put, the final expressed quantities $\boldsymbol{a}$ and by extension the DDSCS are expressed as a ratio to the energy-integrated total scattering, $d\sigma/d\Omega$.

3.2 Recovering the double-differential X-ray scattering cross section

The recorded spectra were down-sampled to an energy pixel resolution of 0.56 eV and area-normalized to unity to preserve the correlation to the scattering ratio. Using the scattering ratio of filtered to unfiltered azimuthal averages and the area-normalized spectra discussed previously, a ridge regression was used to solve for $\boldsymbol{a}$ with $\lambda = 1.5$ to mitigate nonphysical regression artifacts. Figure 6 shows the result of the spectral ghost-imaging process for the range of scattering angles. Since the dominant portion of the scattering signal stems from the elastic scattering, $\Delta E = 0$, the primary feature in Fig. 6 is a signature of the zinc K-edge itself. q-dependent features are evident above the convolved edge, consistent with inelastic scattering contributions to the signal.

The ghost-imaged quantity, $\boldsymbol{a}$, represents the dynamic structure factor convolved with the zinc absorption spectrum. Therefore, if the filter function $f(E_\mathrm{s})$ is known, $\boldsymbol{a}$ can be deconvolved to determine the DDSCS. As the inelastic X-ray scattering signal tends to zero at low momentum transfer, we can recover $f(E_\mathrm{s})$ from $a(q,E_\mathrm{i})$ by taking its limit as $q \rightarrow 0$. A non-negative least-squares regression was used to deconvolve the filter function in Eq. (15) to recover the scattering spectrum, shown in Fig. 7.

Due to the limited bandwidth of the X-ray pulses, the high-fidelity portions of the $\boldsymbol{a}$ vectors were limited. Following the deconvolution, this has the effect of combining any scattering with an energy loss greater than the bandwidth of the incident pulses into the final bins of the reconstructed scattering spectrum. Since

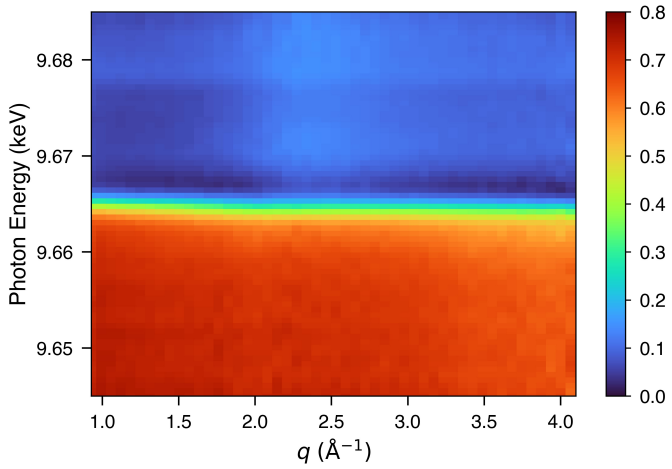

Fig. 6 Ghost-imaged $\boldsymbol{a}$-vectors. The edge-shaped feature at 9.665 keV is the impression of the zinc K-edge and the elastic scattering. q-dependent features exist above the edge, indicative of inelastic scattering. Due to the ratio of scattering used in the ghost-imaging analysis, the values of $\boldsymbol{a}$ are unitless.

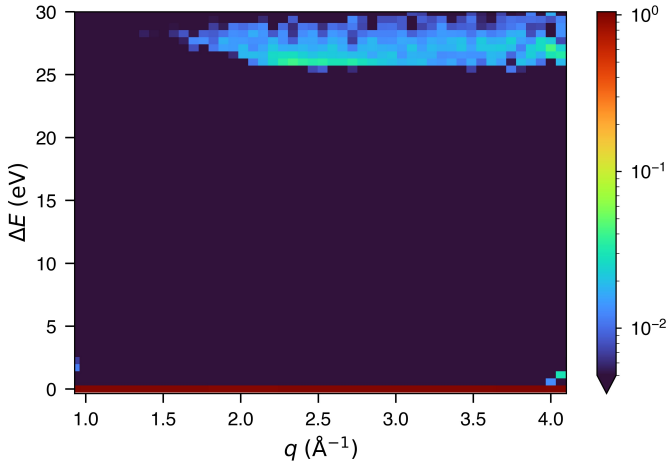

Fig. 7 Recovered Bethe surface of SF_6. Here, the dynamic structure factor has been normalized by the total scattering profile. The elastic scattering, seen at $\Delta E = 0$ eV, encompass a single bin, demonstrating the spectral resolution. The Compton scattering is summed into the feature near $\Delta E = 27$ eV. The featureless region in between is reflective of insufficient statistics for recovering the onset of the Compton peak and the bound-to-bound inelastic transitions.

View Article Online
DOI: 10.1039/D6FD00068A

the pulse bandwidth is ~25 eV, the maximum energy loss that can be resolved is ~25 eV. Therefore, any inelastic scattering that occurs at $\Delta E > 25$ eV is compressed into the largest reconstructible energy loss bins.

The ghost imaging technique successfully decomposes the total scattering into the DDSCS. The elastic scattering is almost completely contained within a single energy bin at $\Delta E = 0$. In the inelastic regime, there is no visible signal except for a large feature at $\Delta E = 25$ eV, representing a sum of the vast majority of inelastic scattering, resolved in q. This feature is attributed to Compton scattering. The Compton signal should start at ~15 eV, close to the ionization potential of SF_6. However, very few electrons contribute to the Compton scattering in the interval 15–25 eV, and thus the signal is much weaker compared to the sum of the Compton scattering signal above $\Delta E = 25$ eV. In addition, transitions between bound-to-bound states should be present as q-dependent features in the range of 1–15 eV as depicted in Fig. 1 for H_2O. This signal should appear as a series of peaks that converge in intensity to the Compton scattering at 15 eV. However, due to the limitations of the experiment, we were unable to reconstruct the scattering spectrum with high enough signal-to-noise to recover these features. Evidently, these bound-to-bound inelastic features are dwarfed by the Compton scattering above $\Delta E = 25$ eV.

While current generation XFELs are capable of delivering $\sim 10^{12}$ photons per pulse and thus allow for the spectrally resolved X-ray scattering experiments, we are still limited to samples with large scattering cross sections, such as SF_6. While this affords a high signal-to-noise ratio for the total scattering signal, it has the consequence of decreasing the fraction of individual inelastic elements with respect to the total X-ray scattering signal, consistent with Fig. 7.

Improvements can be made to the method. As stated in Section 2.3, fluorescence from the zinc foil needed to be accounted for. While the corrections did remove the majority of the impact, they may inflict new errors. Also, the Jungfrau-4M does have a rough energy sensitivity, but is not sensitive enough for separation of the zinc fluorescence from the scattering. In addition, individual photons incident on the detector can trigger more than one pixel, distributing their energy across them. Photon counting could be used to remedy this, but those algorithms are only effective when the number of photon strikes per pixel per image are $\lesssim 1$. In this experiment, there are a large number of incident photons per pixel per image at low scattering angles and a small number at high scattering angles. This suggests a hybrid continuous/discrete approach, counting photon strikes to identify and filter out fluorescence counts at high scattering, while using the fluorescence method shown here in the continuous, low scattering angle regime.

4 Conclusions

We have demonstrated a spectral ghost-imaging technique that enables the model-independent spectral decomposition of the total X-ray scattering signal of gas-phase molecules using a conventional energy-integrating area detector at an XFEL. By exploiting the inherent shot-to-shot spectral stochasticity of SASE pulses in conjunction with a thin zinc foil acting as a spectral filter and a pre-specimen single shot spectrometer, the scattering spectrum of SF_6 was measured at the LCLS.

The methodology presented here is general and not limited to static systems. In a pump-probe experiment, the same spectral ghost-imaging approach could be applied to time-resolved X-ray scattering experiments, enabling simultaneous and accurate tracking of structural dynamics through the elastic scattering signal and the associated electronic spectrum *via* the inelastic scattering. Given the rich information about excited states that can already be inferred from elastic or total scattering alone,[47–50] it is clear that such measurements would provide an unprecedented window into the coupled nuclear and electronic landscape that governs photochemical processes, charge transfer, and non-adiabatic transitions in general.

A key limitation of the present work is the counting statistics afforded by the 120 Hz repetition rate of the LCLS. The ghost-imaging reconstruction relies on correlating the stochastic spectral fluctuations across many pulses. The fidelity and precision of the reconstructions, particularly across the relatively weak bound-to-bound transition and onset of Compton scattering regions, is directly tied to the number of independent measurements. The upcoming LCLS-II-HE, operating at repetition rates in the kHz regime, will dramatically increase the rate of data collection and provide large improvements in counting statistics. This will not only allow for increased spectral resolution of the recovered DDSCS, but will make this technique more feasible for weakly scattering targets and time-resolved experiments where the available signal per time-delay bin is inherently less. These advances position spectral-ghost imaging as a powerful and broadly applicable technique for the next generation of gas-phase X-ray scattering experiments at high-repetition rate XFELs.

Author contributions

Conceptualization: P.M.W. Formal Analysis: D.J.R., B.H.S., A.M.C., P.Y.W., M.S., A.K., P.M.W. Funding Acquisition: A.K., P.M.W. Investigation: D.J.R., A.N.J., L.H., S.W.C., X.C., M.L., S.M., M.P.M., P.M.W. Methodology: P.M.W. Project Administration: P.M.W. Resources: D.J.R., J.G., X.C., M.L., S.M., M.P.M., A.K., P.M.W. Software: D.J.R., A.M.C., P.Y.W., M.S., P.M.W. Supervision: D.J.R., A.K., P.M.W. Validation: D.J.R., B.H.S., A.M.C., M.S. Visualization: D.J.R., B.H.S., A.M.C., M.S. Writing – original draft: D.J.R., B.H.S., A.M.C., M.S., A.K., P.M.W. Writing – review & editing: D.J.R., B.H.S., A.M.C., M.S., A.K., P.M.W.

Conflicts of interest

There are no conflicts to declare

Data availability

Experimental data is available upon request.

Acknowledgments

PMW acknowledges stimulating discussions with Uwe Bergmann (U. Wisconsin, Madison), Hasan Yavas and Daniel F. Ratner (SLAC National Laboratory). This research was supported by the National Science Foundation, Award No. CHE-2309434 (DJR, ANJ), the U.S. Department of Energy, Office of Science, Basic

View Article Online
DOI: 10.1039/D6FD00068A

Energy Sciences, Award No. DE-SC0017995 (LH) and the U.S. Department of Energy, Office of Science, Basic Energy Sciences, Award No. DE-SC0020276 (BHS, SWC). Use of the Linac Coherent Light Source (LCLS), SLAC National Accelerator Laboratory, is supported by the U.S. Department of Energy, Office of Science, Office of Basic Energy Sciences under Contract No. DE-AC02-76SF00515. This work was supported by the National Institutes of Health grant S10 OD025079. AK acknowledges funding from the UK Engineering and Physical Sciences Research Council (EPSRC), grants EP/V049240/2, EP/X026698/1, and EP/X026973/1, and the Leverhulme Trust grant RPG-2020-208. PYW acknowledges a DPhil studentship from the University of Oxford. This work used the resources of the SLAC Shared Science Data Facility (S3DF) at SLAC National Accelerator Laboratory. S3DF is a shared High-Performance Computing facility, operated by SLAC, that supports the scientific and data-intensive computing needs of all experimental facilities and programs of the SLAC National Accelerator Laboratory. SLAC is operated by Stanford University for the U.S. Department of Energy's Office of Science.

References

1 A. Odate, A. Kirrander, P. M. Weber and M. P. Minitti, *Advances in Physics: X*, 2023, **8**, 2126796.

2 B. Stankus, H. Yong, J. Ruddock, L. Ma, A. M. Carrascosa, N. Goff, S. Boutet, X. Xu, N. Zotev, A. Kirrander, M. Minitti and P. M. Weber, *J. Phys. B*, 2020, **53**, 234004.

3 L. Young, K. Ueda, M. Gühr, P. H. Bucksbaum, M. Simon, S. Mukamel, N. Rohringer, K. C. Prince, C. Masciovecchio, M. Meyer, A. Rudenko, D. Rolles, C. Bostedt, M. Fuchs, D. A. Reis, R. Santra, H. Kapteyn, M. Murnane, H. Ibrahim, F. Légaré, M. Vrakking, M. Isinger, D. Kroon, M. Gisselbrecht, A. L'Huillier, H. J. Wörner and S. R. Leone, *Journal of Physics B: Atomic, Molecular and Optical Physics*, 2018, **51**, 032003.

4 H. Yong, N. Zotev, J. M. Ruddock, B. Stankus, M. Simmermacher, A. M. Carrascosa, W. Du, N. Goff, Y. Chang, D. Bellshaw, M. Liang, S. Carbajo, J. E. Koglin, J. S. Robinson, S. Boutet, M. P. Minitti, A. Kirrander and P. M. Weber, *Nature Communications*, 2020, **11**, 2157.

5 H. Yong, A. Moreno Carrascosa, L. Ma, B. Stankus, M. P. Minitti, A. Kirrander and P. M. Weber, *Faraday Discussions*, 2021, **228**, 104–122.

6 T. Northey, A. Kirrander and P. M. Weber, *Journal of Synchrotron Radiation*, 2024, **31**, 303–311.

7 B. Stankus, H. Yong, N. Zotev, J. M. Ruddock, D. Bellshaw, T. J. Lane, M. Liang, S. Boutet, S. Carbajo, J. S. Robinson, W. Du, N. Goff, Y. Chang, J. E. Koglin, M. P. Minitti, A. Kirrander and P. M. Weber, *Nature Chemistry*, 2019, **11**, 716–721.

8 B. Stankus, J. M. Budarz, A. Kirrander, D. Rogers, J. Robinson, T. J. Lane, D. Ratner, J. Hastings, M. P. Minitti and P. M. Weber, *Faraday Discussions*, 2016, **194**, 525–536.

9 M. Minitti, J. Budarz, A. Kirrander, J. Robinson, D. Ratner, T. Lane, D. Zhu, J. Glownia, M. Kozina, H. Lemke, M. Sikorski, Y. Feng, S. Nelson, K. Saita, B. Stankus, T. Northey, J. Hastings and P. Weber, *Physical Review Letters*, 2015, **114**, 255501.

10 J. M. Budarz, M. P. Minitti, D. V. Cofer-Shabica, B. Stankus, A. Kirrander, J. B. Hastings and P. M. Weber, *Journal of Physics B: Atomic, Molecular and Optical Physics*, 2016, **49**, 034001.

11 I. Gabalski, M. Sere, K. Acheson, F. Allum, S. Boutet, G. Dixit, R. Forbes, J. M. Glownia, N. Goff, K. Hegazy, A. J. Howard, M. Liang, M. P. Minitti, R. S. Minns, A. Natan, N. Peard, W. O. Rasmus, R. J. Sension, M. R. Ware, P. M. Weber, N. Werby, T. J. A. Wolf, A. Kirrander and P. H. Bucksbaum, *The Journal of Chemical Physics*, 2022, **157**, 164305.

12 H. Yong, N. Zotev, B. Stankus, J. M. Ruddock, D. Bellshaw, S. Boutet, T. J. Lane, M. Liang, S. Carbajo, J. S. Robinson, W. Du, N. Goff, Y. Chang, J. E. Koglin, M. D. J. Waters, T. I. Sølling, M. P. Minitti, A. Kirrander and P. M. Weber, *The Journal of Physical Chemistry Letters*, 2018, **9**, 6556–6562.

13 P. H. Bucksbaum, M. R. Ware, A. Natan, J. P. Cryan and J. M. Glownia, *Physical Review X*, 2020, **10**, 011065.

14 W. Schülke, *Electron Dynamics by Inelastic X-Ray Scattering*, Oxford Science Publications, 1st edn, 2007.

15 M. Simmermacher, P. M. Weber and A. Kirrander, *Structural Dynamics with X-ray and Electron Scattering*, Royal Society of Chemistry, United Kingdom, 2023, vol. 25, ch. 3, pp. 85–125.

16 A. M. Carrascosa and A. Kirrander, *Phys. Chem. Chem. Phys.*, 2017, **19**, 19545–19553.

17 L. Ma, N. Goff, A. M. Carrascosa, S. Nelson, M. Liang, X. Cheng, H. Yong, I. Gabalski, L. Huang, S. W. Crane, A. E. Green, F. Allum, P. Lenzen, S. B. Muvva, L. F. Heald, Y. Liu, S. Bhattacharyya, K. A. Larsen, M. Graßl, R. Forbes, M. Centurion, T. J. A. Wolf, A. Kirrander, M. P. Minitti and P. M. Weber, *Journal of Physics B: Atomic, Molecular and Optical Physics*, 2024, **57**, 205602.

18 A. Moreno Carrascosa, H. Yong, D. L. Crittenden, P. M. Weber and A. Kirrander, *Journal of Chemical Theory and Computation*, 2019, **15**, 2836–2846.

19 N. Zotev, A. M. Carrascosa, M. Simmermacher and A. Kirrander, *J. Chem. Theory Comput.*, 2020, **16**, 2594–2605.

20 A. Moreno Carrascosa, J. P. Coe, M. Simmermacher, M. J. Paterson and A. Kirrander, *Phys. Chem. Chem. Phys.*, 2022, **24**, 24542–24552.

21 R. C. Ulsh, H. F. Wellenstein and R. A. Bonham, *J. Chem. Phys.*, 1974, **60**, 103–111.

22 A. B. Trofimov and J. Schirmer, *Journal of Physics B: Atomic, Molecular and Optical Physics*, 1995, **28**, 2299.

23 T. H. Dunning, Jr., *The Journal of Chemical Physics*, 1989, **90**, 1007–1023.

24 R. A. Kendall, T. H. Dunning, Jr. and R. J. Harrison, *The Journal of Chemical Physics*, 1992, **96**, 6796–6806.

25 K. Kaufmann, W. Baumeister and M. Jungen, *Journal of Physics B: Atomic, Molecular and Optical Physics*, 1989, **22**, 2223.

26 H. Bethe, *Ann. Phys.*, 1930, **397**, 325–400.

27 N. Watanabe, Y. Kamata, K. Yamauchi, Y. Udagawa and T. Müller, *Molecular Physics*, 2004, **102**, 649–657.

28 C. Tavard, M. Rouault and M. Roux, *J. Chim. Phys.*, 1965, **62**, 1410–1417.

View Article Online
DOI: 10.1039/D6FD00068A

29 R. A. Bonham, *Scanning Microscopy*, 1990, **4**, 1991–2001.
30 D. Rich, D. Zhu, J. Turner, D. Zhang, B. Hill and Y. Feng, *Journal of Synchrotron Radiation*, 2016, **23**, 3–9.
31 S. Boutet and G. J Williams, *New Journal of Physics*, 2010, **12**, 035024.
32 Y. Feng, J. M. Feldkamp, D. M. Fritz, M. Cammarata, R. Aymeric, C. Caronna, H. T. Lemke, D. Zhu, S. Lee, S. Boutet, G. Williams, K. Tono, M. Yabashi and J. B. Hastings, X-ray Lasers and Coherent X-ray Sources: Development and Applications IX, 2011, pp. 163–168.
33 J. Wang and V. H. Smith Jr, *Int. J. Quantum Chem.*, 1994, **52**, 1145–1151.
34 G. D. Purvis, III and R. J. Bartlett, *The Journal of Chemical Physics*, 1982, **76**, 1910–1918.
35 T. B. Pittman, Y. H. Shih, D. V. Strekalov and A. V. Sergienko, *Physical Review A*, 1995, **52**, 3429–3432.
36 D. V. Strekalov, A. V. Sergienko, D. N. Klyshko and Y. H. Shih, *Physical Review Letters*, 1995, **74**, 3600–3603.
37 R. S. Bennink, S. J. Bentley and R. W. Boyd, *Physical Review Letters*, 2002, **89**, 1–4.
38 B. I. Erkman and J. H. Shapiro, *Advances in Optics and Photonics*, 2010, **2**, 405–450.
39 J. H. Shapiro and R. W. Boyd, *Quantum Information Processing*, 2012, **11**, 949–993.
40 K. W. C. Chan, M. N. O'Sullivan and R. W. Boyd, *Physical Review A—Atomic, Molecular, and Optical Physics*, 2009, **79**, 033808.
41 N. D. Hardy and J. H. Shapiro, *Physical Review A—Atomic, Molecular, and Optical Physics*, 2011, **84**, 063824.
42 A. Meda, A. Caprile, A. Avella, I. Ruo Berchera, I. P. Degiovanni, A. Magni and M. Genovese, *Applied Physics Letters*, 2015, **106**, 262405.
43 P. Ryczkowski, M. Barbier, A. T. Friberg, J. M. Dudley and G. Genty, *Nature Photonics*, 2016, **10**, 167–170.
44 C. Amiot, P. Ryczkowski, A. T. Friberg, J. M. Dudley and G. Genty, *Optics letters*, 2018, **43**, 5025–5028.
45 X. Qiu, D. Zhang, T. Ma, F. Lin, H. Guo, W. Zhang and L. Chen, *Advanced Quantum Technologies*, 2020, **3**, 2000073.
46 D. Ratner, J. P. Cryan, T. J. Lane, S.Li and G. Stupakov, *Physical Review X*, 2019, **9**, 011045.
47 A. Kirrander, *J. Chem. Phys.*, 2012, **137**, 154310.
48 T. Northey, N. Zotev and A. Kirrander, *J. Chem. Theory Comput.*, 2014, **10**, 4911.
49 M. Simmermacher, N. E. Henriksen, K. B. Møller, A. Moreno Carrascosa and A. Kirrander, *Physical Review Letters*, 2019, **122**, 073003.
50 A. Moreno Carrascosa, M. Yang, H. Yong, L. Ma, A. Kirrander, P. M. Weber and K. Lopata, *Faraday Discussions*, 2021, **228**, 60–81.

View Article Online
DOI: 10.1039/D6FD00068A

Data availability statement

The data stream from the X-ray scattering experiments are archived at SLAC National Laboratory. Analyzed data are available from the authors on request.